ELSEVIER

Contents lists available at ScienceDirect

Journal of Hydrology

journal homepage: www.elsevier.com/locate/jhydrol



Research papers

Underlying riparian lithology controls redox dynamics during stage-driven mixing

Corey D. Wallace*, Mohamad Reza Soltanian

Department of Geology, University of Cincinnati, Cincinnati, OH, USA



This manuscript was handled by Huaming Guo, Editor-in-Chief, with the assistance of Kenneth C. Carroll. Associate Editor

Keywords:
Hyporheic
Redox
Surface water-groundwater interactions
Geochemistry
Groundwater



The interactions between surface water-groundwater (hyporheic) exchange and sediment lithology influence oxidation–reduction (redox) conditions near river-aquifer interfaces. Redox dynamics have implications for subsurface nutrient transformations, but are difficult to assess spatially and temporally using traditional geochemical observations. This study applied continuous, three-dimensional monitoring of redox potential in a shallow riparian aquifer to assess the geochemical response to sediment lithology and hydrogeologic variables. We mapped a series of cross-sectional redox contour plots from throughout the aquifer over a storm event, which captured the dynamics of redox conditions during stage-driven mixing. Results show that redox potential increased by over 400 mV at some locations following river water infiltration during the storm, while persistent zones of high potential endured along preferential, high-conductivity flow paths. Conditions within high-conductivity (>1 cm/s) sediments took longer to recover (up to 30 days) following storms than those within finer, low-conductivity (6.9×10^{-5} cm/s) sediments (days to hours), however, attributed to less organic matter driving nutrient transformations. Dynamic surface water-groundwater interactions intermittently perturb redox conditions, but the underlying sediment lithology ultimately governs the spatial and temporal dynamics of aquifer redox conditions. These novel observations provide fundamental insights into hyporheic exchange and riparian geochemical dynamics broadly applicable to hydrogeology and biogeochemistry.

1. Introduction

Groundwater quality and the associated geochemical state of subsurface systems are becoming increasingly important as global population expands, land-use changes, and contaminants of emerging concern become more ecologically abundant. A number of physical, chemical, and biological processes affect the evolution of aquifer geochemistry (see review papers by Hubbard et al., 2018; Li et al., 2017 summarizing these coupled and complex processes), but perhaps most important are the spatial distributions of hydraulic conductivity (K) and organic matter related to sediment heterogeneity. As hydraulically connected high-K facies (three-dimensional (3D) bodies of sediment (e.g., Soltanian and Ritzi, 2014; Liu et al., 2020)) act as preferential pathways for groundwater flow and nutrient transport under varying flow regimes driven by the local hydraulic gradient, sediment organic matter fuels transformative microbial reactions (e.g., Duff and Triska, 1990; Wallace et al., 2020a). As a result, discrete biogeochemical hot spots (i.e., zones of enhanced reaction rates) may develop throughout the subsurface where conditions favor nutrient transformations (Krause et al., 2017; McClain et al., 2003). Most often these conditions reflect a balance between nutrient availability, flow path residence times, and reaction rates (Bardini et al., 2012; Marzadri et al., 2012; Sawyer, 2015; Wallace et al., 2020b). In aquifers adjacent to rivers, surface water-groundwater (hyporheic) exchange drives the flux of water and solutes across the sediment–water interface and through the subsurface. As channel water from rivers and streams is diverted along deeper hyporheic flow paths and into the adjacent riparian aquifer, it mixes with groundwater and is exposed to geochemically and microbially active sediment surfaces where nutrient transformations may take place (Boano et al., 2010; Cardenas et al., 2015; Harvey et al., 2013; Xu et al., 2017). The hyporheic zone thus serves as an important transition zone for lotic system function, where biogeochemical activity can be locally elevated due inpart to surface water-groundwater mixing.

Due to the high spatial and temporal variability of subsurface flow and solute transport patterns, a fundamental understanding of aquifer geochemical dynamics requires high-resolution information about chemical fluxes and the associated groundwater chemistry. Conventional methods (e.g., core drilling, groundwater sampling) provide

E-mail address: wallacy@ucmail.uc.edu (C.D. Wallace).

^{*} Corresponding author.

insight about discrete locations within the aquifer (e.g., Harms and Grimm, 2008; Peterjohn and Correll, 1984), but the difficulty of collecting such samples at high spatial or temporal resolution and the related costs can inhibit observations of dynamic reaction rates and chemical fluxes. Alternatively, oxidation-reduction (redox) potential can be continuously monitored using relatively inexpensive in-situ sensors. Redox potential (EH) indicates the energetic favorability of a given reaction, and has been used to describe the potential for degradation of anthropogenic contaminants in aquifers (Lensing et al., 1994; McMahon and Chapelle, 2008; Wallace et al., 2018). When monitored continuously, redox data can be a powerful tool for studying the effects of dynamic conditions on metal availability (Vorenhout et al., 2004), nitrogen transformation (Sawyer et al., 2014; Wallace et al., 2018), degradation of organic compounds (Klüpfel et al., 2014; LaRowe and Cappellen, 2011), and other riparian buffer processes (Briggs et al., 2013, 2015; Snyder et al., 2004). Redox potential is related to the concentration of oxidants and reductants in the pore water (e.g., Hinkle et al., 2001; Hsu et al., 2010) and is known to vary with sediment lithology (Carlyle and Hill, 2001; Hill and Cardaci, 2004; King et al., 2019), but heretofore has only been sparsely monitored in one or two dimensions. Further, only a handful of studies have focused on redox monitoring during hyporheic mixing (e.g., Briggs et al., 2015; Sawyer et al., 2014; Wallace et al., 2018), which limits its utility for understanding the controlling influence of sediment heterogeneity and its spatial variability on geochemical dynamics during hyporheic exchange.

The main objective of this study is to demonstrate the capability of fully-continuous, 3D redox data for the first time to quantitatively assess

aquifer redox response to static (i.e., sediment heterogeneity) and dynamic (e.g., storms, seasons) forcings. The study site (described in detail below) was specifically instrumented to improve predictive understandings of riparian aquifer dynamics and response to perturbations, and the aquifer is representative of other heterogeneous environments in the surface and near-surface environment termed the Critical Zone. Results could thus be helpful to other studies related to hydrology-driven biogeochemical behavior, such as those in the East River Watershed (Dwivedi et al., 2017; Hubbardet al., 2018), Critical Zone Observatories (Anderson et al., 2008; Brantley et al., 2007; White et al., 2015), the Worldwide Hydrobiogeochemistry Observation Network for Dynamic River Systems (WHONDRS, Stegen et al., 2018), or coastal aquifers (Heiss et al., 2020, 2017; Kreyns et al., 2020; Michael et al., 2005). The novel aspects of this study are as follows: 1) it is conducted at high spatial and temporal resolution in three dimensions across a relatively large spatial scale (hundreds of meters in scale); and 2) it provides fundamental insights into the distribution, size, and persistence of high- and low-EH zones as well as their expansion and contraction during and after hydrologic perturbations. Further, fundamental insights developed through this study should be widely-transferrable because it is conducted in a buried-valley aquifer, representing aquifers widespread across North America.

2. Study site

The study site $(39.23755^\circ N, 84.71252^\circ W)$ is part of the Theis Environmental Monitoring and Modeling Site (TEMMS), located along a

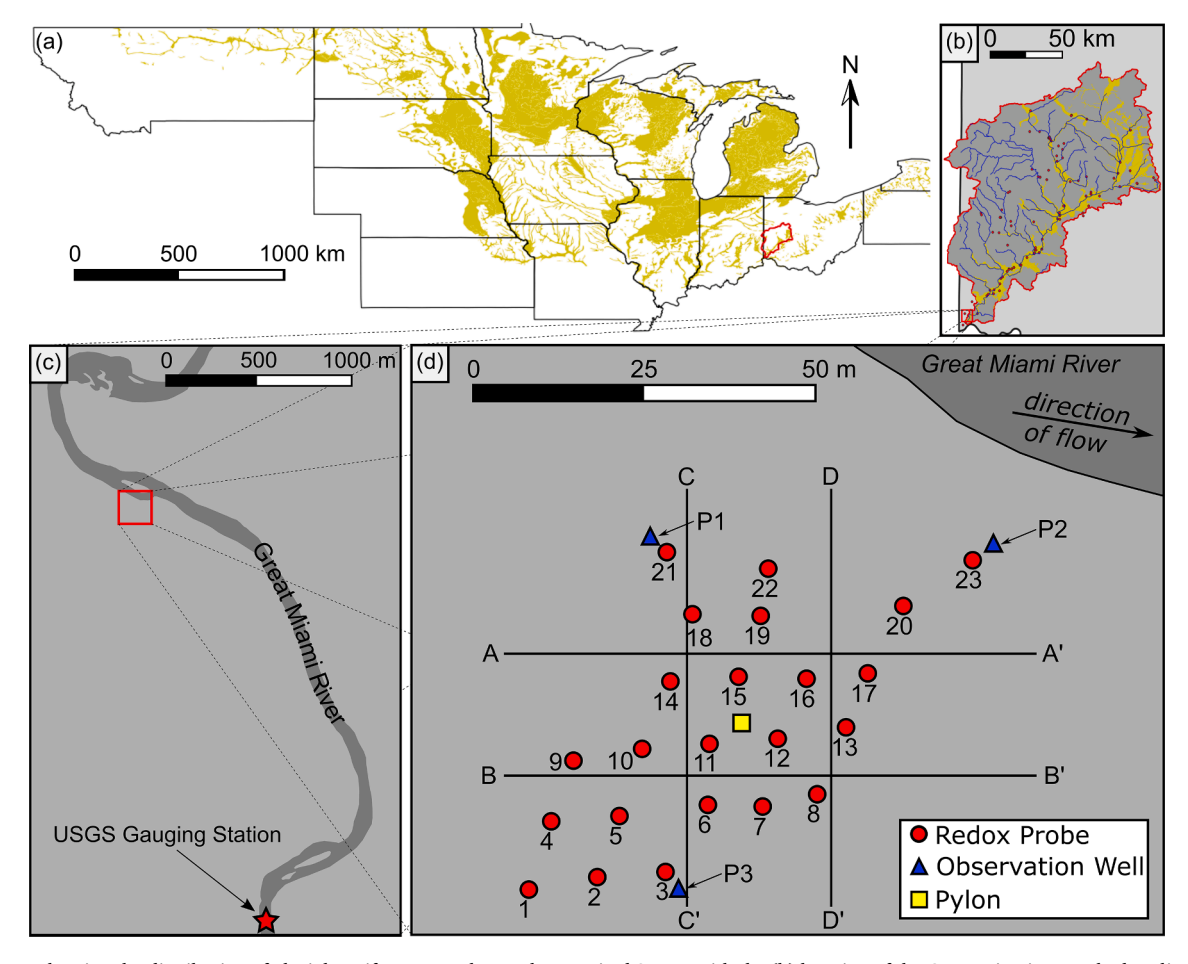


Fig. 1. (a) Map showing the distribution of glacial aquifers across the northern United States, with the (b) location of the Great Miami Watershed outlined in red. (c) The TEMMS is located along a meander of the Great Miami River, and the red star shows the location of a nearby USGS gauge. (d) Instrumentation at the site consists of three pairs of monitoring wells (blue triangles) and a series of 23 redox probes (red circles). Transects for redox analysis (discussed below) are labeled AA', BB', CC', and DD'. (For interpretation of the references to color in this figure legend, the reader is referred to the web version of this article.)

section of the Great Miami River near Cincinnati, Ohio, USA roughly 20 km northwest of downtown Cincinnati (Fig. 1). The Great Miami River is $\sim\!150$ m wide and $\sim\!1.5$ m deep at the study site, and flow averages 110 m³ s $^{-1}$. The channel is generally incised and contains gravelly compound and point bars which represent a larger scale of sedimentary architecture, within which planar and trough cross-bedded sand and gravel are common (Ritzi et al., 2002). The river at the study site is generally losing, and regional groundwater flow through the aquifer is away from the river.

The study aquifer extends roughly 100 m into the southern bank of the Great Miami River, approximately 28 km upstream of its confluence with the Ohio River. The depth to bedrock averages 33 m, and the average water table depth is 5 m below the land surface (Watkins and Spieker, 1971). Aquifer transmissivity is estimated between 1200 and 3700 m 2 d $^{-1}$, with storativity of 0.2 (Spieker, 1968). Sediment lithology at the TEMMS is quite complex, consisting primarily of poorly-sorted, subrounded sediments ranging from cobbles to medium sand with interbedded open-framework gravel (OFG) facies, overlain by ~ 1 m thick, organic-rich silt and clay deposits (Wallace and Soltanian, 2021). The three dominant facies types at the site are fine-grained silt and clay, coarse sand, and gravel.

3. Methods

3.1. Hydrologic and geochemical monitoring

A series of observation wells were installed in 2017 to monitor groundwater levels and basic water quality parameters (Fig. 1). Wells were installed at three locations, and were constructed of 11.5 cm o.d. PVC with 3 m screens. All wells were sealed with granular bentonite and positioned in waterproof concrete pads to prevent preferential flowpaths related to installation. Multiparameter sensors (YSI 600LS) deployed inside each well monitor hydraulic head, temperature, and specific conductance at 15-min intervals. A central pylon houses a weather station (WeatherFlow SKY) to collect data on ambient atmospheric conditions, and a telecommunications link that transmits data from the site every 15 min. River stage is monitored at a nearby USGS gauge (#03274615) located roughly 3 km downstream of the study site. Measurements were extracted to correspond to the on-site data collection period (described below).

Over 90 m of continuous cores (30 m at each of three locations) were collected from the site during well installation to determine sediment properties and constrain floodplain sediment heterogeneity. Wallace and Soltanian (2021) visually described the cores for mineral composition, color, and grain size at 5 cm resolution. Based on visual descriptions, they analyzed grain size for 10 representative samples from each core (30 samples total) within the range of 0.037–8 mm using a Gilson SS-15 Sieve Shaker. All of the samples but one had sediments >8 mm, which were further classified to grains sized less than 80 mm.

Redox probes were installed throughout the riparian floodplain on a roughly 10-m grid to capture redox variations influenced by sediment heterogeneity and a range of water table fluctuations (Fig. 1). Final probe locations were subject to accessibility (i.e., trees, foliage) and local sediment properties (i.e., coarse gravel preventing installation). Each of the 23 probes consisted of a 150-cm fiberglass-epoxy tube embedded with an array of 4 platinum electrodes spaced 45 cm apart (Paleo Terra, Amsterdam, Netherlands). Platinum electrode redox probes do not require calibration, and have been successfully used in variably-saturated systems to describe hydrogeochemical changes in the near-stream environment (e.g., Sawyer et al., 2014; Wallace et al., 2018). All probes were connected to one of two Ag/AgCl reference electrodes installed below the water table in wells P2 and P3. To minimize agitation of the soil layer, we augured to varying depths at each location and then manually inserted the probes an additional 150 cm into undisturbed sediments and backfilled with soil. All sensors were connected to CR800 control modules and AM416 multiplexers

(Campbell Scientific, Logan, UT) and programmed to collect readings every 15 min. All parameters (i.e., $E_{\rm H}$, water table elevation, temperature, specific conductance) were monitored continuously from January 29, 2020 through July 15, 2020.

3.2. Aquifer-Scale redox interpolation

The spatial distribution of E_H throughout the aquifer was calculated using radial basis function interpolation of the redox point measurements (1.7 mV accuracy), which has been shown to provide high-order accurate interpolants of large datasets (Schaback, 1995). A series of unique functions (ϕ_i), each of which possess radial symmetry about one of the sample points, were developed for point readings obtained from the redox probes. A continuous function f, which represents the sum of the individual functions, was then employed to approximate values between the sample points:

$$f(x, y, z) = \sum_{i=1}^{n} c_i e^{-(\varepsilon r)^2}$$
 (1)

where c_i is a fitting coefficient applied to the inverse multiquadratic function ϕ_b n is the number of observed points, and ε is a shape parameter. Coefficients are determined by constraining f to match samples values at the sensor locations. The distance from the central point of each function (r) is defined as:

$$r = \sqrt{(x_i - x_j)^2 + (y_i - y_j)^2 + (z_i - z_j)^2}$$
 (2)

where (x_i, y_i, z_i) denotes the center of the function (i.e., the sample point) and (x_j, y_j, z_j) denotes a field point. Vertical anisotropy often associated with buried-valley sediment stratigraphy was incorporated by scaling z-coordinates by a factor of 0.1, which accounted for the difference between points in the vertical direction when computing r. The resulting interpolation is often spectrally accurate, and stable for large numbers of data points (Buhmann and Dyn, 1993). Based on our field installation, 92 individual redox readings were collected at each time point. Redox data were interpolated to a grid 51 m long, 68 m wide, and 3.75 m deep to represent our study portion of the shallow floodplain aquifer, with the top boundary elevation corresponding to the floodplain topography. The grid was uniformly discretized with 0.15 m horizontal and vertical resolution $(3.85 \times 10^6 \text{ grid cells})$.

The performance of radial basis function interpolation is often dependent on both the type of radial basis functions employed and the associated value of ε for those functions (Rippa, 1999). Not only should the function suit the application for spatial interpolation, but ε should be optimized for the dataset to increase accuracy while maintaining numerical stability. Here, we employ the inverse multiquadratic (IMQ) radial basis function (RHS of Eq. (1)), which has a high-order rate of convergence and has been shown to perform well in groundwater modeling applications (e.g., Amaziane et al., 2004; Li et al., 2003; Yao et al., 2016). The optimal shape parameter for IMQ functions generally depends on the density and distribution of the observed points, and the interpolated function values at the points (Fasshauer and Zhang, 2007; Huang et al., 2007). We optimized ε by minimizing the root mean squared error (RMSE) of the interpolated dataset relative to the observed redox point measurements (Fig. S1). Using $\varepsilon = 0.03$, the error was reduced to 1.7 mV (less than 0.2% of our range of redox observations).

3.3. Time-Series analysis

The continuous wavelet transform (CWT) was used to characterize the frequency content of time-series data, and to resolve temporal variations in energy at a given frequency related to hydrologic events. Further, the correlation between CWT signals can be used to identify relationships between different time series and provide information about relative signal lag. The Morlet wavelet was used for the CWT

because it is well-localized in space and time, and is thus appropriate for feature extraction (Farge, 1992; Grinsted et al., 2004):

$$\Psi_0(\eta) = \pi^{-1/4} e^{i\omega_0 \eta} e^{-\eta^2/2} \tag{3}$$

where ω_0 is dimensionless frequency ($\omega_0=6$) and η is dimensionless time. The CWT of a time-series x(t) with uniform time steps is then defined as:

$$W_{x,y}(\tau,s) = \int_{-\infty}^{\infty} x(t) \frac{1}{\sqrt{s}} \psi^* \left(\frac{t-\tau}{s}\right) dt \tag{4}$$

where s is the scale of the transformed time-series $W_{x,\psi}(\tau,s)$ at position τ in the time domain, and ψ^* is the complex conjugate of the wavelet function. Edge effects cause errors at the beginning and end of the wavelet power spectrum, as indicated by the shaded regions in CWT images. Wavelet analysis reveals when particular frequencies in a time-series are stronger or weaker, and can be used to resolve the effects of hydrologic perturbations across temporal scales (e.g., Wallace et al., 2018). For example, if a storm affects redox conditions over one week, the CWT plot shows higher power at the one-week frequency during that time

Following CWT analysis of the hydrologic and redox time-series, cross-spectrum analyses (i.e., comparison between the CWT of two signals) of redox with stage and precipitation were used to identify variability within the floodplain. The coherence between CWT signals is a measure of their time-varying correlation, and can be conceptualized as a localized correlation coefficient in time–frequency space. The wavelet coherence of two time series, *X* and *Y*, is defined as (Torrence and Webster, 1999)

$$R_n^2(s) = \frac{|S(s^{-1}w_{XY}(\tau, s)|^2)}{S(s^{-1}|W_X(\tau, s)|^2) \cdot S(s^{-1}|W_Y(\tau, s)|^2)}$$
(5)

where $W_i(s)$ is the wavelet transform of time series i, and S is a smoothing operator represented here by a weighted running average in both the time and scale directions. The interested reader is referred to Torrence and Webster (1999) and Grinsted et al. (2004) for more details about computing the wavelet coherence. The coherence varies between 0 and 1, with higher values indicating when the two signals are more strongly correlated, and phase arrows in correlated regions are used to compute the relative lag time between the two signals (Zhang et al., 2019). For example, high wavelet correlation between river stage and the redox signal during a storm event would result in high coherence over periods of days to weeks (depending on the size of the storm). Shifts in the dominant period(s) over which there is high coherence can also indicate fluctuations across different timescales, and can reveal when the signal is influenced by more than one hydrologic variable (i.e., stage and precipitation). The lag time (Δt) between the signals is calculated as:

$$\Delta t = \frac{\varphi}{360 \cdot f} \tag{6}$$

where φ is the phase angle in degrees and f is the signal frequency (y-axis on cross-spectrum plots). Phase arrows on the cross-spectrum plots point to the right ($\varphi=0^\circ$) when the two signals are in-phase, and to the left ($\varphi=180^\circ$) when the two signals are out-of-phase. To ensure robust analyses, signal lag was only evaluated when wavelet coherence was ≥ 0.85 . Here, we focus the analyses on redox measurements taken within two predominantly high-E $_{\rm H}$ (E $_{\rm H}>700$ mV) and low-E $_{\rm H}$ (E $_{\rm H}<300$ mV) regions of the aquifer. These definitions of high- and low-E $_{\rm H}$ were based on typical redox zonation in groundwater, where potentials above ~ 700 mV correspond to aerobic conditions and potentials below ~ 300 mV represent moderately reducing conditions (e.g., Klüpfel et al., 2014; Wallace et al., 2018). Though the redox response within such regions will vary spatially and temporally across the floodplain depending upon the adjacent heterogeneity structure and proximity to the river, these analyses provide insight into how the relative influence of each

hydrologic parameter varies with sediment heterogeneity.

4. Results and interpretation

4.1. Geohydrologic measurements

Stage changes propagated through the aquifer within a matter of hours, and average amplitudes of water table fluctuations were 59.5%, 64.8%, and 45.1% of the river stage amplitude at locations P1, P2, and P3, respectively (Fig. 2). Sediment core analyses reflect prior reports of interbedded sand and gravel facies overlain by low-K silts and clays (Fig. 3). The hydraulic conductivity of the sediments estimated using Hazen's equation (Hazen, 1892) varied by orders of magnitude, increasing from 6.9×10^{-5} cm/s in the overlying silt facies, to 0.16 cm/s in sand-dominated facies, to just over 1 cm/s in sandy gravel facies (Fig. 3). Grain size analysis was not performed on OFG sediments because some cobbles exceeded 150 mm in diameter and the distribution curve would not have been well-constrained. However, previous work to determine the K of OFG facies measured values as high as 4 cm/s (e.g., Ferriera et al., 2010). Based on Darcy's law, the instantaneous flow rate between the river and groundwater ranged from -4.22 to 1.70 m/d. In general, pore water velocities were greater through the shallow aquifer where the hydraulic gradient was steeper across the bank seepage face. Though near the riverbank (i.e., at locations P1 and P2) the volumes of water infiltrating and exfiltrating were approximately equal, further into the aquifer at location P3 only about 27% of the total Darcy flux during the study period was towards the river.

The immediate aquifer response to stage changes likely indicates preferential flow along connected high-K facies. Specific conductance measurements in wells revealed that during high-stage or flood events, surface water penetrated as far as 100 m laterally into the aquifer. For example, during a significant flood event that occurred from March 19–23, 2020, specific conductance values in wells P1 (\sim 35 m from the stream bank) and P3 (\sim 100 m from the stream bank) both dropped by over 50% in less than 1 h concurrent with a 49% drop in groundwater temperature, suggesting rapid infiltration of relatively fresh surface water along connected groundwater flowpaths (Fig. 4). The water table profiles at both locations also showed very similar responses to the increase in river stage, indicating a high degree of hydraulic connectivity across the aquifer likely caused by spatially connected high-K facies (e. g., gravel, OFG) (Fig. 3).

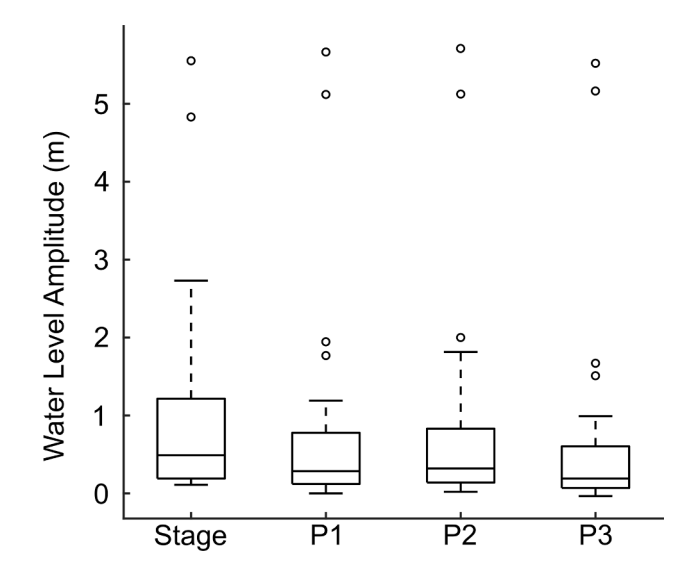


Fig. 2. Boxplot of stage and water table data over the study period showing the range in water level fluctuations in response to storm events. The largest amplitudes are seen in the stage data, and the signal decays moving further into the floodplain.

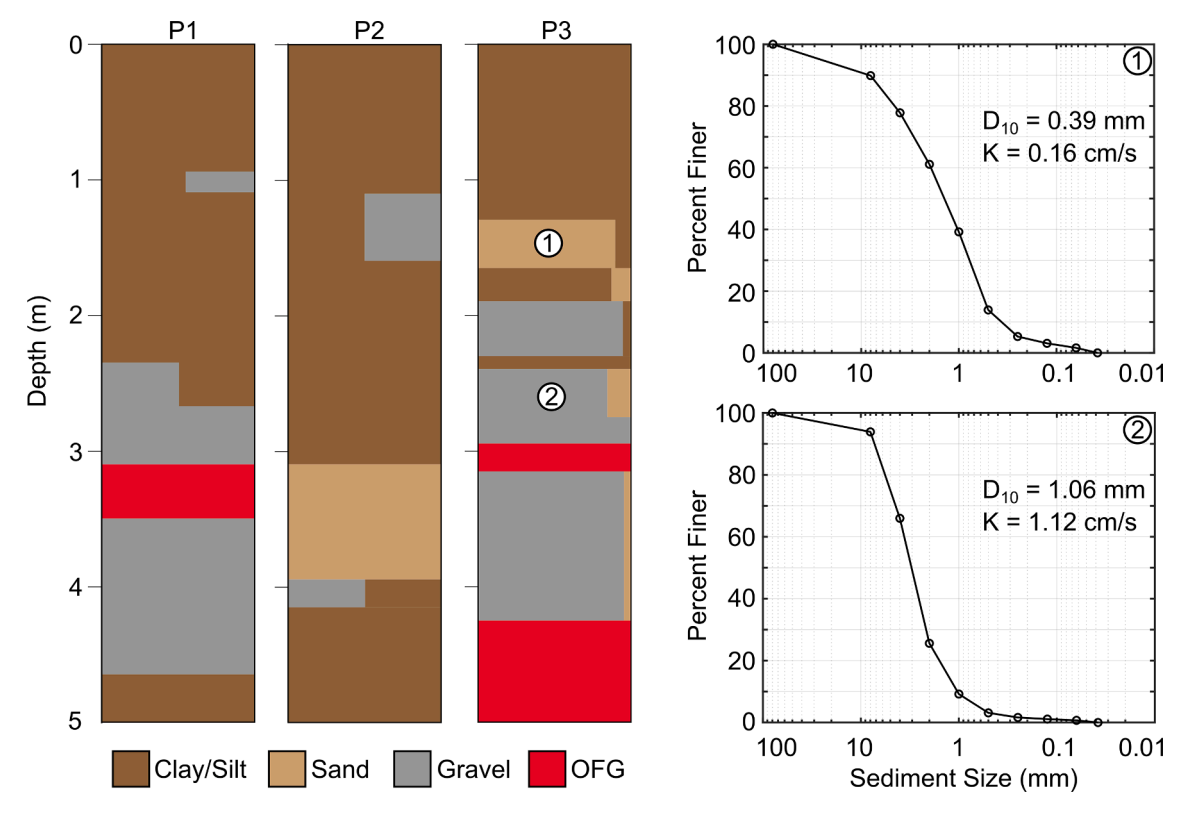


Fig. 3. Sediment cores at locations P1, P2, and P3 show lithologic variation at the depth of redox analysis. Depth increases moving down the columns. The top roughly 1 m of each column consists of silts and clays, underlain by interbedded sands and gravels. Grain size analyses of (1) sand, (2) gravel, and silt (not shown) facies show *K* variability across orders of magnitude, and with some OFG cobbles exceeding 150 mm in diameter.

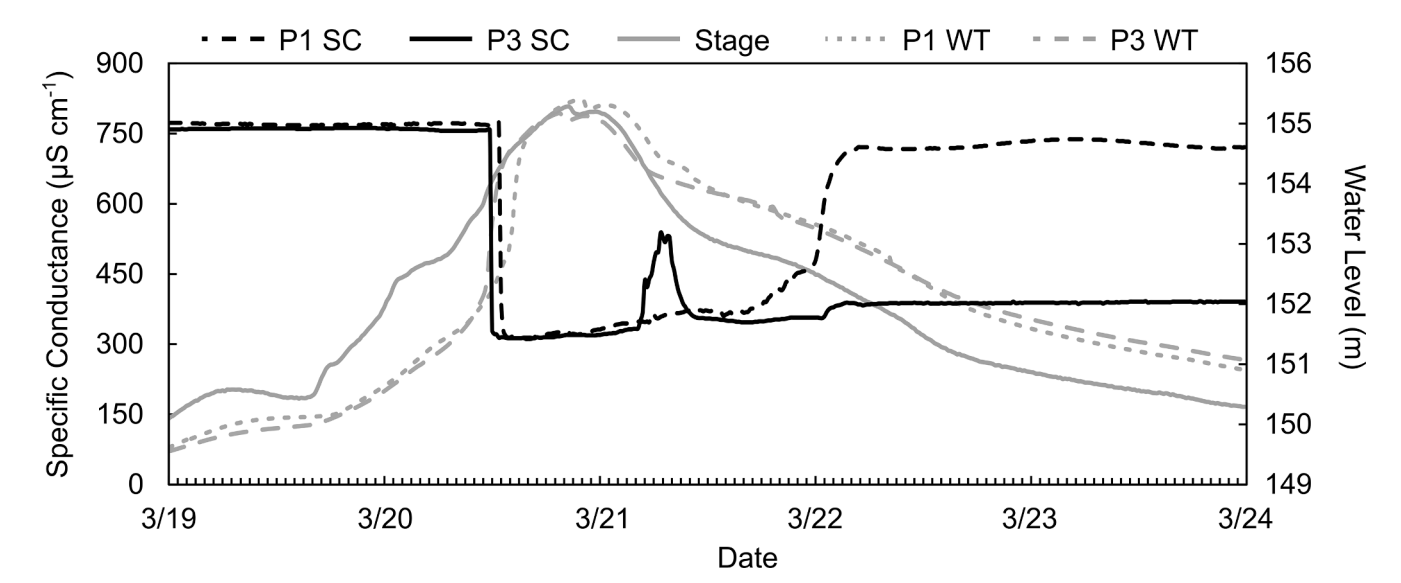


Fig. 4. The response of the specific conductance signal at wells P1 and P3 during a major storm event from March 19–23, 2020 indicate rapid infiltration of surface water. The similar behavior of both the specific conductance signal and water table fluctuations reveal a high degree of hydraulic connectivity across the aquifer.

4.2. Redox potential and redox dynamics

Continuous redox measurements reflect the implicit findings of the basic hydrologic measurements. We first quantified the contributions of changing water temperature on redox measurements. Groundwater temperatures fluctuated between 8.6 and 17.7 $^{\circ}$ C at location P2 and between 6.7 and 13.8 $^{\circ}$ C at location P3, where reference electrodes were installed. The effects of changing temperature on the groundwater redox state were calculated following Sawyer et al. (1995):

$$C = 199 - 1.01 \times (T - 25) \tag{7}$$

where T is the temperature of the groundwater and C is the potential correction used to adjust the raw measured redox potential at each electrode. The temperatures observed near the river at location P2 (available in the metadata) were more variable (coefficient of variation $(C_{\nu}) = 0.27$ °C) over the study period than those further inland at location P3 ($C_{\nu} = 0.18$ °C), suggesting enhanced hyporheic mixing near the river bank. Redox potentials have not been corrected for pH. Redox

measurements can also be affected by the saturation state of the aquifer (e.g., Jennings, 2007; Smith and van Huyssteen, 2011), but water table measurements in this study and previous studies at the TEMMS (e.g., Wallace and Soltanian, 2021) indicate rapid head changes which propagate throughout the aquifer in a matter of hours. Thus, because our redox electrodes are all positioned at nearly the same elevation and within the same soil horizons, we interpret $E_{\rm H}$ changes equally at all locations.

The time-series of redox potentials captures the dynamics of hyporheic mixing, revealing how infiltrating surface water influences subsurface redox conditions. Generally, $E_{\rm H}$ values throughout the aquifer increased immediately following stage rise, corresponding with changes in water table elevation that indicate surface water infiltration. Some centrally-located probes (e.g., probes 12 and 13) showed a higher degree of variability, however, with conditions fluctuating by up to 16% during storms (data available in the metadata). These changes are associated with electrodes positioned within highly conductive facies that quickly convey infiltrating river water. Transects of the subsurface redox potential, two roughly parallel (AA' and BB') and two roughly perpendicular (CC' and DD') to the direction of river flow, clearly show

variation in redox conditions.

Redox conditions varied spatially throughout the study period. Here we focus our analysis around a major storm event that occurred from March 18-21, 2020 as an example of a hydrologic perturbation that induced a significant aquifer redox response (Fig. 5). The first set of contour plots are from March 17, roughly one day before the onset of heavy precipitation. The fourth set of contour plots are from March 21 when the stage was at its peak. The remaining sets of contour plots show the redox profiles on the rising (times 2 and 3) and falling (times 5, 6, and 7) limbs of the hydrograph. The contour plots show increasing E_H throughout the aquifer as stage increased and river water infiltrated, associated with preferential flow pathways formed by hydraulicallyconnected, high-K facies types as indicated by Fig. 4. A deep high-E_H zone on the west side of transect AA' expanded vertically and horizontally with the dynamic river stage, while shallow and deep high-EH zones became vertically connected near the center of transect CC'. The extent of these high-EH zones increased through contour plots 1-4, and contracted afterward. Within a few hours of the maximum stage, the total volume of high-EH sediments within the aquifer increased by almost 300% from $\sim 130 \text{ m}^3$ to $\sim 383 \text{ m}^3$ (Fig. 6).

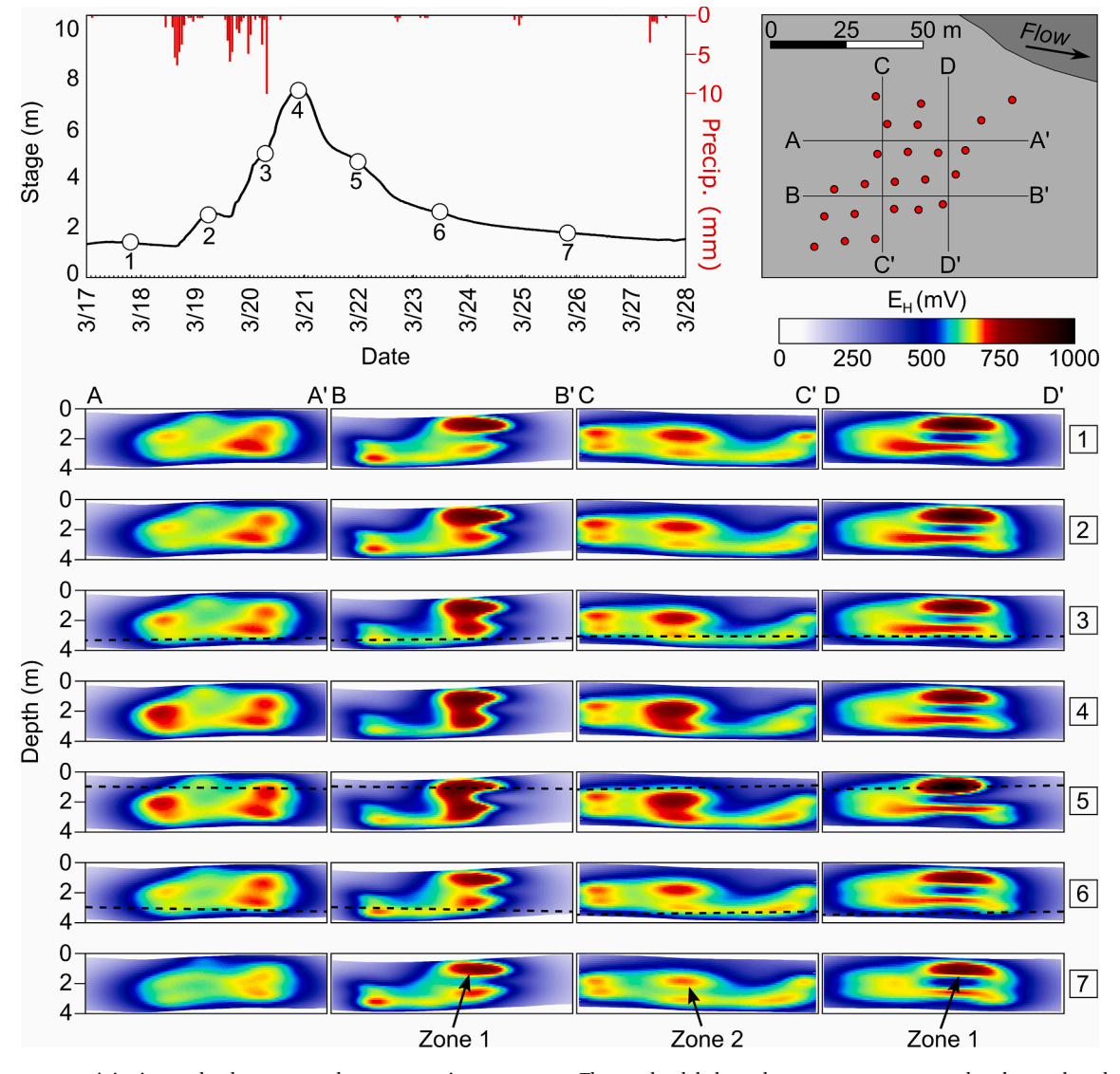


Fig. 5. River stage, precipitation, and redox contour plots over a major storm event. The number labels on the stage curve correspond to the numbered contour plots at transects roughly parallel (AA' and BB') and perpendicular (CC' and DD') to the direction of river flow. Black dashed lines on the contour plots indicate the water table elevation. The water table was below the indicated depth at times 1, 2, and 7, and was above the land surface when the site was flooded at time 4. The persistent, high- $E_{\rm H}$ (>700 mV) zones 1 and 2 are indicated by the black arrows.

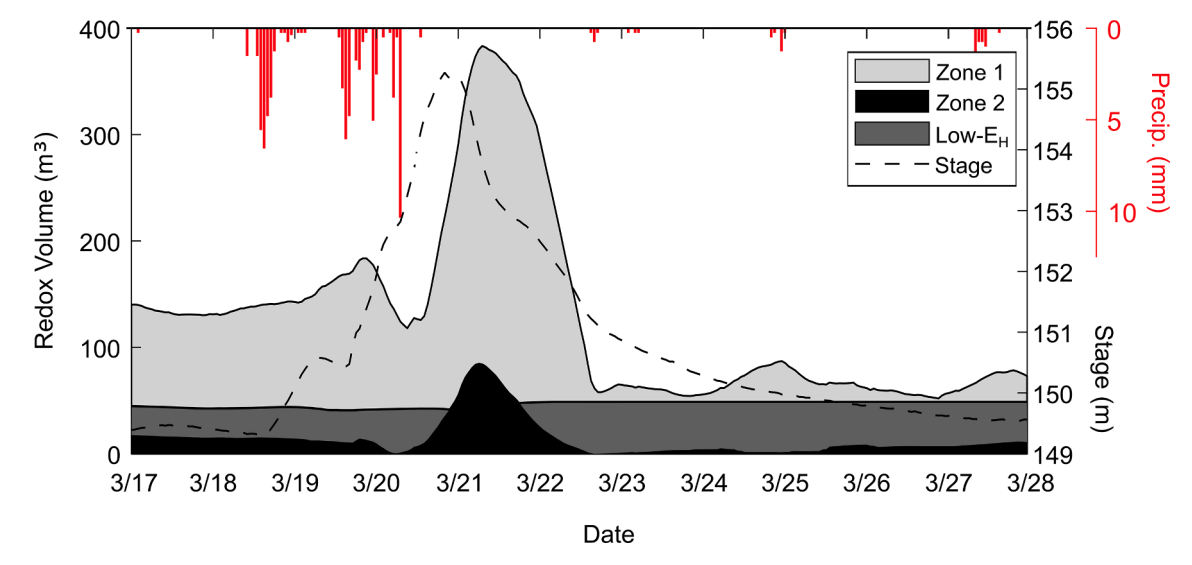


Fig. 6. Time-series of the response of persistent, high- E_H (>700 mV) and low- E_H (<300 mV) volumes to changes in stage and precipitation. The shallow high- E_H zone (Zone 1) was more influenced by precipitation, as seen by its expansion during the storm on May 19–20. Both high- E_H zones expanded following stage rise in response to the storm, increasing the total aquifer high- E_H volume by nearly 300%, while the low- E_H zone showed negligible response to either variable.

Comparing the redox contour plots also shows notable changes in the extent of low- E_H conditions (Fig. 5). As river stage increased between times 1–4, E_H decreased significantly on the west side of transect BB', even as a large high- E_H zone developed towards the center of the transect. Simultaneously, E_H decreased farther from the river at roughly the same depth (\sim 2 m) on the south sides of both transects CC' and DD' perpendicular to the direction of river flow. This suggests that infiltrating river water also displaces relatively low- E_H groundwater and drives redox changes further inland, but further field investigations are needed to substantiate this idea. Such dynamic low- E_H conditions occurred only near dynamic high- E_H regions, however, while other low- E_H regions persisted throughout the aquifer even during the hydrologic perturbation (Fig. 6).

4.3. Redox zonation related to lithology

The redox contour plots show that consistently high-E_H conditions (>700 mV) persisted throughout the study period within two distinct regions of the aquifer, a large region near the center roughly 1 m below the ground (near the intersection of BB' and DD') termed Zone 1, and a smaller region on the western side located roughly 2.5 m below the ground (seen near the center of transect CC') termed Zone 2 (Fig. 5). Though both show consistently high-E_H conditions, their size and shape evolved independently through time and they responded differently to changes in stage and precipitation (Fig. 6). Sediment cores from locations P1 and P3 (Fig. 3) combined with ongoing field observations (i.e., Fig. 4) indicate the presence of high-K and gravel-dominated facies in the shallow aquifer, and cross-comparison with these redox trends suggests that these facies bisect the aquifer at these locations. Bivariate correlation analyses (i.e., the linear correlation between variables, wherein a value of + 1 shows total positive correlation and 0 no correlation) reveal that while both regions were influenced by stage fluctuations ($\rho = 0.69$ and 0.59 for Zones 1 and 2, respectively), precipitation moderately influenced Zone 1 but not Zone 2 ($\rho = 0.19$ and -0.07, respectively). The p-values for all analyses were <0.001. This trend was observed throughout the monitoring period: stage primarily drove elevated E_H conditions, with negligible influence of precipitation except during major storm events which resulted in site flooding.

The distribution of observed changes in redox potential calculated over the study period highlights areas of increased microbial activity and dynamic fluid mixing. The range of redox fluctuations was calculated as the difference between the absolute maximum and minimum $E_{\rm H}$

potential at each point in space over the entire study period (Fig. 7). Redox potential fluctuated throughout the aquifer, with the locations of greatest change often co-located with persistent, high-E_H Zones 1 and 2. For example, the most dynamic conditions were located in a shallow zone near the intersection of transects BB' and DD', which also represents the persistent, shallow high-E_H zone discussed above. Co-location of dynamic vet persistent high-E_H conditions suggests preferential flow paths of higher-K and gravel-dominated facies types. This region was underlain by a broad area where changes in redox potential were small or noticeably absent, however, which corresponds to the deeper, narrow high-E_H zone seen along transect DD' (Fig. 5). This is also interpreted as a preferential flow path, and may even represent a gravel dominated cross-strata (e.g., OFG). Such facies often exhibit unimodal grain size distributions ($d_{50} > 2$ mm) with high K due to a lack of sediment blocking pore spaces between gravel grains (Ferreira et al., 2010; Lunt and Bridge, 2004). Not only does this create rapid and localized dispersion of solutes through the aquifer, but the relative absence of fine, organic-rich sediments may limit the sustained supply of DOC, thereby reducing microbial reaction rates (e.g., Hunter et al., 1998) and limiting reaction extents as DOC sourced from infiltrated river water is rapidly consumed (Wallace et al., 2020b). Further, the reduced surface area of large-grained, high-K sediments relative to fine-grained sediments limits the contact time between nutrients and bioreactive surfaces, further reducing the potential for nutrient transformation. As a result, high-E_H conditions persisted with little change in the redox state caused by microbial activity. Redox conditions were also highly dynamic in the shallow aguifer near the stream bank along transect DD' (Figs. 5, 7), where redox potential fluctuated by roughly 200 mV (21.8% of the total observed range in E_H across the floodplain). This represents a transition zone, where river water and groundwater mix. Other regions with nominal redox fluctuation and consistently low EH are interpreted as mostly hosting anoxic groundwater with little to no mixing (Fig. 6).

Redox data from probes immediately adjacent to wells (i.e., P1, P2, P3) were compared with core data at each location to further evaluate the influence of sediment lithology on redox dynamics (Fig. 7c). The mean facies length of high-K sand or gravel facies in buried-valley aquifers is on the order of meters with a coefficient of variation in length of 1 m (e.g., Ritzi et al., 2002; Dai et al., 2004), thus the lithology observed in cores from P1, P2, and P3 should be representative of the sediment structure associated with redox data collected at probes 21 (2.3 m from P1), 23 (4.1 m from P2), and 3 (2.7 m from P3). In general, redox potential fluctuated most within or near the transition to high-K

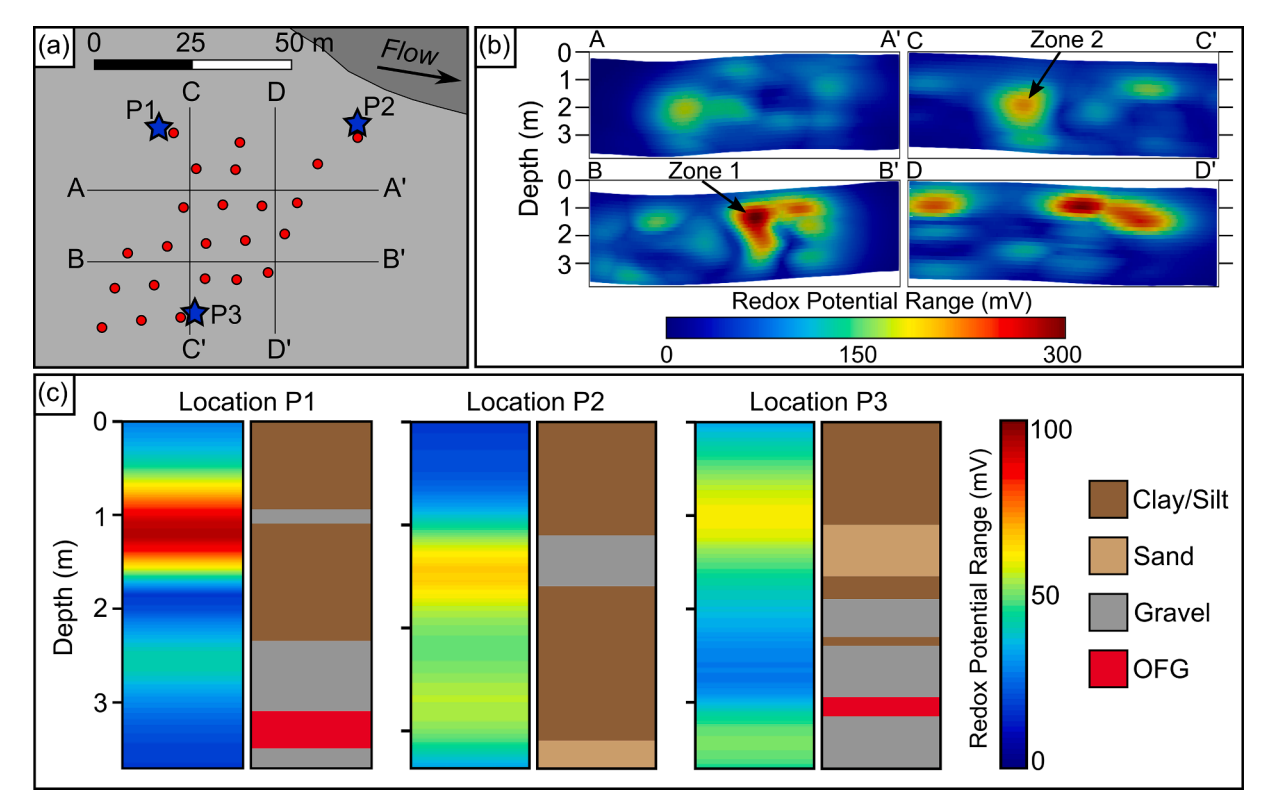


Fig. 7. (a) Site map showing relative locations of redox probes (red circles), core locations (blue stars), and analysis transects. (b) Range in redox potentials over the study period, calculated as the difference between the absolute maximum and minimum potential at each point in space. Dynamic regions of greatest change are often co-located with persistent, high-E_H Zones 1 and 2. (c) Comparison of redox range (left columns) and sediment lithology (right columns) at P1 (redox probe 21), P2 (redox probe 23), and P3 (redox probe 3) reveal the greatest E_H change at or near the transition between low- and high-K sediment layers. (For interpretation of the references to color in this figure legend, the reader is referred to the web version of this article.)

facies (Fig. 7c). At P1, redox potential fluctuated by nearly 100 mV over the study period at roughly 1 m depth, corresponding with a ~ 10 cm interval of gravel interbedded between silt facies. Similarly, a dynamic region roughly 1.5 m deep at P2 is correlated with a $\sim\!50$ cm thick gravel facies. Location P3 also showed some variability despite its distance from the channel, with redox potential fluctuations of up to 60 mV located near the transitions between low-K and high-K facies.

4.4. Temporal dynamics

Cross-wavelet analysis shows that river stage had the greatest influence on redox conditions throughout the aquifer during storm events, but its influence was tempered in low-E_H regions located within lower-K sediments (Fig. 8). The first sizeable storm event on March 18 raised the water table ~ 5.8 m and flooded the site, which considerably changed the aguifer redox state (Figs. 4, 5). A subsequent storm on May 18 raised the water table \sim 5.4 m and also flooded the site, but induced a smaller redox response, which indicates the absence of preferential vertical infiltration from the overlying flood waters into the shallow aquifer which may alter the geochemistry. In general, EH conditions showed a strong response (i.e., high coherence) to significant stage changes caused by storm events. Redox conditions responded differently in lowand high-E_H regions of the aquifer, however. At sensor 4, consistently low-E_H conditions (located in the low-E_H zone in Fig. 6, $\mu=267\pm50$ mV) showed minimal response to stage changes (including the flood event in March) over short time periods, and phase arrows indicate that redox lagged stage by 24 days over longer periods (Fig. 8c). At sensor 14 located just 26 m away, E_H was consistently high (located within Zone 2, $\mu = 682 \pm 40$ mV) and showed a strong response to stage fluctuations, with redox conditions responding to stage changes in roughly 12 h (Fig. 8a). Though precipitation did not consistently influence either

signal, during the large storm event in March redox conditions at sensor 14 lagged the precipitation signal by 3.4 days over a period of 8 days (Fig. 8b). Precipitation negligibly influenced redox conditions in the low-E $_{\rm H}$ region at sensor 4 over the monitoring period (Fig. 8d). High wavelet coherence over short periods (\leq 0.125 days) on the precipitation plots for both zones is likely associated with the spurious correlation of noise characteristic of climatic signals (e.g., Maraun and Kurths, 2004), while high coherence on all plots over periods > 32 days (often associated with seasonal changes) must be interpreted with caution given the length of our datasets.

Our cross-wavelet analyses highlight the significance of interpreting redox variations through the lens of frequency content because they reveal the influence of hydrologic perturbations, which is often concealed by general time series analyses (i.e., Fig. 4). For example, despite the consistently low $E_{\rm H}$ at sensor 4, the potential still fluctuated by up to 75 mV throughout the study period. Cross-wavelet analysis of these data showed that these changes did not occur on the same time-scale as changes in stage or precipitation (as would be expected along connected high-K pathways), however, and so conditions were relatively unperturbed by such hydrologic forcings.

5. Discussion

Subsurface redox conditions are influenced by an assemblage of hydrologic and lithologic variables, including stage fluctuations, precipitation, and sediment heterogeneity. Our results reveal that while redox conditions are intermittently perturbed by temporally-variable environmental changes (i.e., storm surge), the underlying sediment heterogeneity ultimately governs the formation and persistence of high-and low-E_H zones. Given that fine sediments (i.e., clays, silts) typically have a higher organic matter content than their high-K counterparts (i.

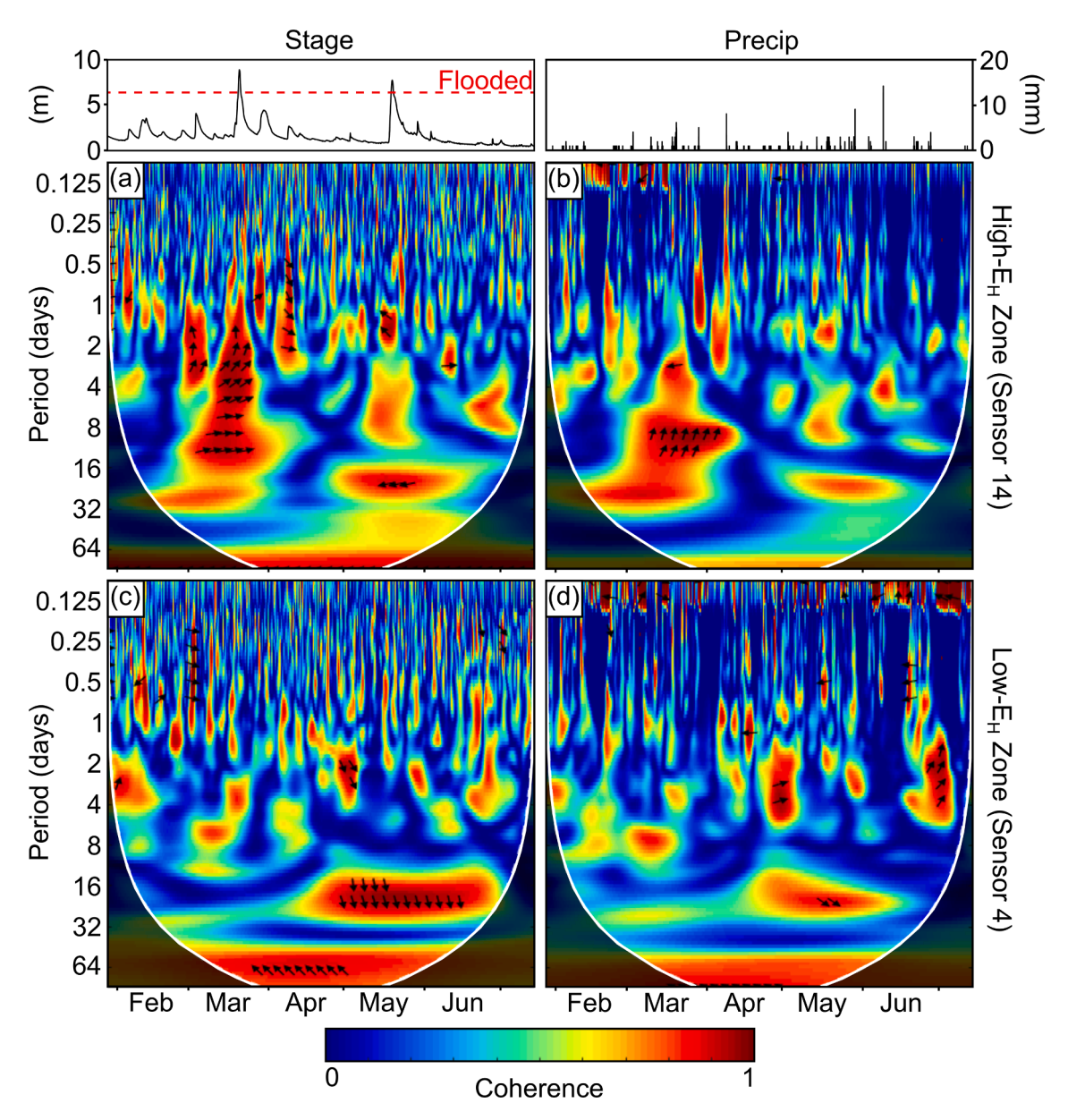


Fig. 8. Cross-spectrum plots of redox signal within high- E_H (top) and low- E_H (bottom) zones at sensors 14 and 4 within the TEMMS floodplain, respectively. Redox signal was compared to river stage (a, c) and precipitation (b, d). Regions of high coherence are shown in red, and phase arrows indicate the lag between redox and water level signals. Stage (left) and precipitation (right) time-series are shown above wavelet plots for comparison. (For interpretation of the references to color in this figure legend, the reader is referred to the web version of this article.)

e., sandy gravel and OFG), reaction hotspots are more likely to form within such impermeable facies than along preferential flow pathways (Newcomer et al., 2018). Our high-resolution observations of subsurface redox zonation likely represent an end-member example given the complex sediment heterogeneity inherent to glacial aquifers, but similar redox patterns have been observed in other heterogeneous coastal (e.g., Seybold et al., 2002, Wallace et al., 2018) and non-coastal (e.g., King et al., 2019) environments. The geochemical state of subsurface systems, and the associated efficiency of subsurface nutrient cycling, are thus tied to sediment lithology, and their complexity is not well-represented by two-dimensional monitoring.

Despite the vast growth in observational data documenting riparian processes, many observations represent discrete measurements which are difficult to interpret through time. Also, these observations are not usually made during storm events (hydrologic perturbations). This represents a deficiency for vulnerable regions where continuous monitoring could elucidate controls on groundwater quality, especially those

related to large research community networks such as the Critical Zone Observatories, USGS Hydrologic Benchmark Network, and the Great Lake Ecological Observatory Network. The utility of continuous, 3D redox monitoring for assessing hydrology-driven aquifer dynamics thus stems from a lack of understanding about how biogeochemical conditions vary spatially and temporally. Here, across the floodplain E_H consistently showed greater fluctuations along high-K facies and a dampened response to hydrologic perturbations within low-K facies (Figs. 5, 6, 7). Though the glacial aquifer in this study is highly heterogeneous with extremely high K due to the presence of graveldominated facies types such as OFG, redox zonation and E_H variability are observed to follow similar trends in other systems with lower contrasts in K and less hydraulic connectivity (e.g., Wallace et al., 2018). Coupling redox monitoring with the extensive observational infrastructure available at many sites (e.g., Carnevali et al., 2020; Dwivedi et al., 2018b) would help characterize spatial variability, and significantly improve predictive understandings of biogeochemical processes

and their response to perturbations.

Hydrodynamics such as stage fluctuations exerted an important control on subsurface redox conditions, and the duration and lag time of perturbations revealed the interplay between transport and kinetic (reaction) controls on the geochemistry. In high-K, high-EH regions of the aquifer, redox conditions responded quickly to changes in river stage, similar to observations within other heterogeneous aquifers (e.g., Lahiri and Davidson, 2020; Su et al., 2018). Though water and nutrients were delivered efficiently along high-K flowpaths, the absence of fine, organic-rich sediments likely inhibited microbial respiration and nutrient transformation. As a result, it took longer (on the order of weeks) for equilibrium to be reestablished (Fig. 8). Further, rapid temperature fluctuations associated with river water infiltration would presumably play an important role in nutrient transformation as reaction kinetics (and redox conditions) adjusted accordingly (Massmann et al., 2006; Munz et al., 2019; Seybold et al., 2002). Conversely, low-EH conditions showed a delayed response to changes in river stage as local, low-K and high organic matter sediments (in our case silt, clay, and siltysand) created barriers to flow and nutrient delivery. However, because the high organic carbon content of the sediments bolstered respiration rates, the redox signal typically recovered within a matter of days. These findings are consistent with other studies discussing the importance of lithology on subsurface redox conditions (e.g., King et al., 2019; Sawyer et al., 2014; Wallace et al., 2018), but our results further demonstrate and quantify the importance of small-scale spatial differences in geochemistry caused by local changes in sediment properties. When coupled with chemical data, these analyses may also help constrain reaction kinetics and reveal implications for groundwater nutrient and contaminant remediation and transformation, especially during dynamic hydrologic perturbations that bolster flow and solute delivery throughout the subsurface.

The dynamics of subsurface redox zonation indicate where and when conditions are most favorable for redox-driven solute transformations, but information about the groundwater chemistry is needed for further assessment. Our goal to assess the lithologic and hydrologic controls on subsurface redox conditions did not require analysis of groundwater chemistry, but such data in combination with redox monitoring represents a powerful tool for identifying and quantifying reaction specific biogeochemical hotspots. Future work at the TEMMS will therefore involve not only spatially-distributed groundwater sampling, but 16S rRNA gene sequencing and quantification of sediment organic matter content to evaluate subsurface nutrient cycling and contaminant transformation.

A few other techniques allow for assessment of geochemical conditions related to sediment lithology. An increasingly popular approach is the use of time-lapse electrical resistivity tomography (ERT) and induced polarization (IP), which have been applied both in coastal and non-coastal environments (e.g., Cardenas and Markowski, 2010; Kessouri et al., 2019; Ntarlagiannis et al., 2005; Nyquist et al., 2008). However, such geophysical methods are often costly, and their accuracy depends strongly on the inversion method used to process the data. Further, their efficacy may be limited depending on the specific degradation processes involved, which could underestimate the degree of subsurface redox shifts. We presented only an example application of 3D in-situ redox monitoring, but this technique can be used to spatially assess subsurface redox conditions across a broad range of timescales. Not only are the sensors relatively inexpensive and straightforward to use (McMahon and Chapelle, 2008), but platinum redox electrodes are rather durable, often functioning reliably for long periods in both oxic and anoxic conditions (Shoemaker et al., 2013; Swerhone et al., 1999).

6. Conclusions

We have shown that redox conditions in floodplain sediments are strongly perturbed by dynamic stage-driven mixing events that intensify hyporheic exchange and solute transport, but the influence of such hydrologic perturbations is ultimately controlled by the underlying sediment lithology. Redox conditions are highly dynamic along high-*K* facies which act as preferential flowpaths during river water infiltration, while low-*K* facies temper redox dynamics by limiting flow and the exchange of complimentary solutes. Redox monitoring allows for geochemical investigation when consistent sampling is difficult, or where sites are inaccessible during large storms, and the regular sampling interval permits frequency analysis to parse out the relative influence of storms or other hydrologic forcings. By providing a continuous and time-lapse record of subsurface conditions, 3D in-situ redox measurements can be used to understand the control of sediment heterogeneity on the reactive transport of redox-sensitive solutes in hydrodynamic environments.

CRediT authorship contribution statement

Corey D. Wallace: Conceptualization, Methodology, Data curation, Formal analysis, Investigation, Writing - original draft, Writing - review & editing. **Mohamad Reza Soltanian:** . : Conceptualization, Methodology, Investigation.

Declaration of Competing Interest

The authors declare that they have no known competing financial interests or personal relationships that could have appeared to influence the work reported in this paper.

Acknowledgments

This study was funded by the National Science Foundation (EAR-PF 1855193) and the University of Cincinnati through faculty startup fund to the second author. The Theis Environmental Monitoring and Modeling Site was built with funding from the University of Cincinnati, the Duke Energy Foundation, and the Miami Conservancy District on land provided by Great Parks of Hamilton County. We thank Tyler McGarr for assistance in the field, and David Nash for designing a publicly-available data interface which provides real-time readings of hydrologic conditions at the site. The free tool is available online at https://cvtheisgwo.artsci.uc.edu/. All time series data are available on website CUAHSI HydroShare (https://doi.org/10.4211/ hs.4d3f5cbbc1cd480cb9ca4f0d56240e4f). This manuscript benefited from the feedback of two anonymous reviewers.

Appendix A. Supplementary data

Supplementary data to this article can be found online at https://doi.org/10.1016/j.jhydrol.2021.126035.

References

Amaziane, B., Naji, A., Ouazar, D., 2004. Radial basis function and genetic algorithms for parameter identification to some groundwater flow problems. CMC 1 (2), 117–128.

Anderson, S.P., Bales, R.C., Duffy, C.J., 2008. Critical Zone Observatories: Building a network to advance interdisciplinary study of Earth surface processes. Mineralogical Magazine 72 (1), 7–10. https://doi.org/10.1180/minmag.2008.072.1.7.

Bardini, L., Boano, F., Cardenas, M.B., Revelli, R., Ridolfi, L., 2012. Nutrient cycling in bedform induced hyporheic zones. Geochim. Cosmochim. Acta 84, 47–61. https:// doi.org/10.1016/j.gca.2012.01.025.

Boano, F., Demaria, A., Revelli, R., Ridolfi, L., 2010. Biogeochemical zonation due to intrameander hyporheic flow. Water Resour. Res. 46, 1–13. https://doi.org/ 10.1029/2008WR007583.

Brantley, S.L., Goldhaber, M.B., Ragnarsdottir, K.V., 2007. Crossing disciplines and scales to understand the critical zone. Elements 3 (5), 307–314. https://doi.org/10.2113/ gselements.3.5.307.

Briggs, M.A., Day-Lewis, F.D., Zarnetske, J.P., Harvey, J.W., 2015. A physical explanation for the development of redox microzones in hyporheic flow. Geophys. Res. Lett. 42, 4402–4410. https://doi.org/10.1002/2015GL064200.

Briggs, M.A., Lautz, L.K., Hare, D.K., Gonzalez-Pinzon, R., 2013. Relating hyporheic fluxes, residence times, and redox-sensitive biogeochemical processes upstream of beaver dams. Freshwater. Science 33 (2). https://doi.org/10.1899/12-110.1.

- Buhmann, M., Dyn, N., 1993. Spectral convergence of multiquadric interpolation. Proc. Edinburgh Math. Soc. 36 (2), 319–333.
- Cardenas, M.B., 2015. Hyporheic zone hydrologic science: A historical account of its emergence and prospectus. Water Resour. Res. 51 (5), 3601–3616. https://doi.org/ 10.1002/2015WR017028.
- Cardenas, M.B., Markowski, M.S., 2010. Geoelectrical imaging of hyporheic exchange and mixing of river water and groundwater in a large regulated river. Environ. Sci. Technol. 45, 1407–1411. https://doi.org/10.1021/es103438a.
- Carlyle, G.C., Hill, A.R., 2001. Groundwater phosphate dynamics in a river riparian zone: effects of hydrologic flowpaths, lithology and redox chemistry. J. Hydrol. 247, 151–168.
- Carnevali, P.B.M., Lavy, A., Thomas, A.D., Crits-Christoph, A., Diamond, S., Meeheust, R., Olm, M. R., Sharrar, A., Lei, S., Dong, W., Falco, N., Bouskill, N., Newcomer, M., Nico, P., Wainwright, H., Dwivedi, D., Williams, K.H., Hubbard, S., Banfield, J.F., 2020. Meanders as a scaling motif for understanding of floodplain soil microbiome and biogeochemical potential at the watershed scale. bioRxiv. https://doi.org/10.1101/2020.05.14.086363.
- Dai, Z., Ritzi, R.W., Dominic, D.F., 2004. Estimating parameters for hierarchical permeability correlation models. SEPM Special Publication 80, 41–54.
- Duff, J.H., Triska, F.J., 1990. Denitrification in sediments from the hyporheic zone adjacent to a small forested stream. Can. J. Fish. Aquat. Sci. 47, 1140–1147.
- Dwivedi, D., Steefel, C., Arora, B., Bisht, G., 2017. Impact of intra-meander hyporheic flow on nitrogen cycling. Proc. Earth Planet. Sci. 17, 404–407. https://doi.org/ 10.1016/j.proeps.2016.12.102.
- Dwivedi, D., Steefel, C. I., Arora, B., Newcomer, M., Moulton, J. D., Dafflon, B., Faybishenko, B., Fox, P., Nico, P., Spycher, N., Carroll, R., Williams, K.H., 2018. Geochemical exports to river from the intrameander hyporheic zone under transient hydrologic conditions: east river mountainous watershed, Colorado. Water Resour. Res. 54(10). https://doi.org/10.1029/2018WR023377.
- Farge, M., 1992. Wavelet transforms and their application to turbulence. Annu. Rev. Fluid Mech. 24, 395–457.
- Fasshauer, G.E., Zhang, J.G., 2007. On choosing "optimal" shape parameters for RBF approximation. Numer Algor 45, 345–368.
- Ferreira, R.V., Cerqueira, M.A., de Melo, M.T., de Figueiredo, D.R., Keizer, J.J., 2010. Spatial patterns of surface water quality in the Cértima River basin, central Portugal. J. Environ. Monit. 12 (1), 189–199. https://doi.org/10.1039/b914409a.
- Grinsted, A., Moore, J.C., Jevrejeva, S., 2004. Application of the cross wavelet transform and wavelet coherence to geophysical time series. Nonlinear Processes Geophys. 11, 561–566.
- Harms, T.K., Grimm, N.B., 2008. Hot spots and hot moments of carbon and nitrogen dynamics in a semiarid riparian zone. J. Geophys. Res. 113 (G01020), 1–14. https://doi.org/10.1029/2007JG000588.
- Harvey, J.W., Bohlke, J.K., Voytek, M.A., Scott, D., Tobias, C.R., 2013. Hyporheic zone denitrification: Controls on effective reaction depth and contribution to wholestream mass balance. Water Resour. Res. 49, 6298–6316. https://doi.org/10.1002/ wrcr.20492.
- Hazen, A., 1892. Some Physical Properties of Sands and Gravels, with Special Reference to their Use in Filtration (24th Annual Report, Issue.
- Heiss, J.W., Michael, H., a., & Puleo, J., 2020. Groundwater-surface water exchange in the intertidal zone detected by hydrologic and coastal oceanographic measurements. Hydrol. Process. 34 (17), 3718–3721. https://doi.org/10.1002/hyp.13825.
- Heiss, J.W., Post, V.E.A., Laattoe, T., Russoniello, C.J., Michael, H.A., 2017. Physical controls on biogeochemical processes in intertidal zones of beach aquifers. Water Resour. Res. 53, 9225–9244. https://doi.org/10.1002/2017WR021110.
- Hill, A.R., Cardaci, M., 2004. Denitrification and Organic Carbon Availability in Riparian Wetland Soils and Subsurface Sediments. Soil Sci. Soc. Am. J. 68, 320–325.
- Hinkle, S.R., Duff, J.H., Triska, F.J., Laenen, A., Gates, E.B., Bencala, K.E., Wentz, D.A., Silva, S.R., 2001. Linking hyporheic flow and nitrogen cycling near the Willamette River - a larger river in Oregon, USA. J. Hydrol. 244, 157–180. https://doi.org/ 10.1016/S0022-1694(01)00335-3.
- Hsu, C.-H., Han, S.-T., Kao, Y.-H., Liu, C.-W., 2010. Redox characteristics and zonation of arsenic-affected multi-layers aquifers in the Choushui River alluvial fan, Taiwan. J. Hydrol. 391, 351–366. https://doi.org/10.1016/j.jhydrol.2010.07.037.
- Huang, C.-S., Lee, C.-F., Cheng, A.H.-D., 2007. Error estimate, optimal shape factor, and high precision computation of multiquadric collocation method. Eng. Anal. Boundary Elem. 31, 614–623. https://doi.org/10.1016/j. enganabound.2006.11.011.
- Hubbard, S.S., Williams, K.H., Agarwal, D., Banfield, J., Beller, H., Bouskill, N., Brodie, E., Carroll, R., Dafflon, B., Dwivedi, D., Falco, N., Faybishenko, B., Maxwell, R., Nico, P., Steefel, C., Steltzer, H., Tokunaga, T., Tran, P. A., Wainwright, H., Varadharajan, C., 2018. The East River, Colorado, Watershed: a mountainous community testbed for improving predictive understanding of multiscale hydrological-biogeochemical dynamics. Vadose Zone J. 17(1), 1–25. https://doi.org/10.2136/vzj2018.03.0061.
- Hunter, K.S., Wang, Y., Van Cappellen, P., 1998. Kinetic modeling of microbially-driven redox chemistry of subsurface environments: coupling transport, microbial metabolism and geochemistry. J. Hydrol. 209, 53–80. https://doi.org/10.1016/ S0022-1694(98)00157-7.
- Jennings, K., 2007. Effect of Varying Degrees of Water Saturation on Redox Conditions in a Yellow Brown Apedal B Soil Horizon University of the Free State]. Bloemfontein, South Africa.
- Kessouri, P., Furman, A., Huisman, J. A., Martin, T., Mellage, A., Ntarlagiannis, D., Mucker, M., Ehosioke, S., Fernandez, P., Flores-Orozco, A., Kemna, A., Nguyen, F., Pilawski, T., Saneiyan, S., Schmutz, M., Schwartz, N., Weigand, M., Wu, Y., Zhang, C., Placencia-Gomez, E., 2019. Induced polarization applied to biogeophysics: recent advances and future prospects. Near Surface Geophys. 17(6), 595-621. https://doi.org/10.1002/nsg.12072.

- King, E.K., Thompson, A., Pett-Ridge, J.C., 2019. Underlying lithology controls trace metal mobilization during redox fluctuations. Sci. Total Environ. 665, 1147–1157. https://doi.org/10.1016/j.scitotenv.2019.02.192.
- Klüpfel, L., Piepenbrock, A., Kappler, A., Sander, M., 2014. Humic substances as fully regenerable electron acceptors in recurrently anoxic environments. Nat. Geosci. 7, 195–200. https://doi.org/10.1038/NGEO2084.
- Krause, S., Lewandowski, J., Grimm, N.B., Hannah, D. M., Pinay, G., McDonald, K., Marti, E., Argerich, A., Pfister, L., Klaus, J., Battin, T., Larned, S. T., Schelker, J., Fleckenstein, J., Schmidt, C., Rivett, M. O., Watts, G., Sabater, F., Sorolla, A., Turk, V., 2017. Ecohydrological interfaces as hot spots of ecosystem processes. Water Resour. Res. 53(8), 6359-6376. https://doi.org/10.1002/2016WR019516.
- Kreyns, P., Geng, X., Michael, H.A., 2020. The influence of connected heterogeneity on groundwater flow and salinity distributions in coastal volcanic aquifers. J. Hydrol. 586 https://doi.org/10.1016/j.jhydrol.2020.124863.
- Lahiri, C., Davidson, G.R., 2020. Heterogeneous oxygenation of wetland soils with increasing inundation: Redox potential, water depth, and preferential flow paths. Hydrol. Process. 34, 1350–1358. https://doi.org/10.1002/hyp.13654.
- LaRowe, D.E., Van Cappellen, P., 2011. Degradation of natural organic matter: A thermodynamic analysis. Geochim. Cosmochim. Acta 75, 2030–2042. https://doi. org/10.1016/j.gca.2011.01.020.
- Lensing, H.J., Vogt, M., Herrling, B., 1994. Modeling of biologically mediated redox processes in the subsurface. J. Hydrol. 159, 125–143.
- Li, J., Chen, Y., Pepper, D., 2003. Radial basis function method for 1-D and 2-D groundwater contaminant transport modeling. Comput. Mech. 32, 10–15. https://doi.org/10.1007/s00466-003-0447-y.
- Li, L., Maher, K., Navarre-Sitchler, A., Druhan, J., Meile, C., Lawrence, C., Moore, J., Perdrial, J., Sullivan, P., Thompson, A., Jin, L., Bolton, E.W., Brantley, S.L., Dietrich, W.E., Mayer, K.U., Steefel, C.I., Valocchi, A., Zachara, J., Kocar, B., Mcintosh, J., Tutolo, B. M., Kumar, M., Sonnenthal, E., Bao, C., Beisman, J., 2017. Expanding the role of reactive transport models in critical zone processes. Earth-Sci. Rev. 165, 280-301. https://doi.org/10.1016/j.earscirev.2016.09.001.
- Liu, Y., Wallace, C.D., Zhou, Y., Ershadnia, R., Behzadi, F., Dwivedi, D., Xue, L., Soltanian, M.R., 2020. Influence of streambed heterogeneity on hyporheic flow and sorptive solute transport. Water 12 (6). https://doi.org/10.3390/w12061547.
- Lunt, I.A., Bridge, J.S., 2004. Evolution and deposits of a gravelly braid bar, Sagavanirktok River, Alaska. Sedimentology 51, 415–432. https://doi.org/10.1111/ j.1365-3091.2004.00628.x.
- Maraun, D., Kurths, J., 2004. Cross wavelet analysis: significance testing and pitfalls. Nonlinear Processes Geophys. 11, 505–514. https://doi.org/10.5194/npg-11-505-2004.
- Marzadri, A., Tonina, D., Bellin, A., 2012. Morphodynamic controls on redox conditions and on nitrogen dynamics within the hyporheic zone: Application to gravel bed rivers with alternate-bar morphology. Biogeosciences 117 (G3).
- Massmann, G., Greskowiak, J., Dunnbier, U., Zuehlke, S., Knappe, A., Pekdeger., 2006. The impact of variable temperatures on the redox conditions and the behaviour of pharmaceutical residues during artifical recharge. J. Hydrol. 328, 141–156. https://doi.org/10.1016/j.jhydrol.2005.12.009.
- McClain, M.E., Boyer, E.W., Dent, C.L., Gergel, S.E., Grimm, N.B., Groffman, P.M., Hart, S.C., Harvey, J.W., Johnston, C.A., Mayorga, E., McDowell, W.H., Pinay, G., 2003. Biogeochemical Hot Spots and Hot Moments at the Interface of Terrestrial and Aquatic Ecosystems. Ecosystems, 6, 301-312. https://doi.org/10.1007/s10021-003-0161-9.
- McMahon, P.B., Chapelle, F.H., 2008. Redox Processes and Water Quality of Selected Principal Aquifer Systems. Groundwater 46 (2), 259–271. https://doi.org/10.1111/i.1745-6584.2007.00385.x
- Michael, H.A., Mulligan, A.E., Harvey, C.F., 2005. Seasonal oscillations in water exchange between aquifers and the coastal ocean. Nature 436 (7054), 1145–1148. https://doi.org/10.1038/nature03935
- Munz, M., Oswald, S.E., Schafferling, R., Lensing, H.-J., 2019. Temperature-dependent redox zonation, nitrate removal and attenuation of organic micropollutants during bank filtration. Water Res. 162, 225–235. https://doi.org/10.1016/j. watres.2019.06.041.
- Newcomer, M.E., Hubbard, S.S., Fleckenstein, J.H., Maier, U., Schmidt, C., Thullner, M., Ulrich, C., Flipo, N., Rubin, Y., 2018. Influence of Hydrological Perturbations And Riverbed Sediment Characteristics On Hyporheic Zone Respiration of CO2 and N2. J. Geophys. Res. Biogeosci. 123, 902–922. https://doi.org/10.1002/2017JG004090.
- Ntarlagiannis, D., Williams, K.H., Slater, L., Hubbard, S., 2005. Low-frequency electrical response to microbial induced sulfide precipitation. J. Geophys. Res. – Biogeosci. 110 (G2), 1–12. https://doi.org/10.1029/2005JG000024.
- Nyquist, J.E., Freyer, P.A., Toran, L., 2008. Stream bottom resistivity tomography to map ground water discharge. Groundwater 46 (4). https://doi.org/10.1111/j.1745-6584.2008.00432.x.
- Peterjohn, W.T., Correll, D.L., 1984. Nutrient dynamics in an agricultural watershed: observations on the role of a riparian forest. Ecology 65 (5), 1466–1475.
- Rippa, S., 1999. An algorithm for selecting a good value for the parameter c in radial basis function interpolation. Adv. Comput. Math. 11, 193–210.
- Ritzi, R.W., Dai, Z., Dominic, D.F., Rubin, Y.N., 2002. Spatial Structure of Permeability in Relation to Hierarchical Sedimentary Architecture in Buried-Valley Aquifers: Centimeter to Kilometer Scales. Bridging the Gap Between Measurement and Modeling in Heterogeneous Media International Groundwater Symposium, Berkeley, CA
- Sawyer, A.H., 2015. Enhanced removal of groundwater-borne nitrate in heterogeneous aquatic sediments. Geophys. Res. Lett. 42, 403–410. https://doi.org/10.1002/2014G1062234
- Sawyer, A.H., Kaplan, L.A., Lazareva, O., Michael, H.A., 2014. Hydrologic dynamics and geochemical responses within a floodplain aquifer and hyporheic zone during

- Hurricane Sandy. Water Resour. Res. 50, 4877-1892. https://doi.org/10.1002/201
- Sawyer, D.T., Sobkowiak, A., Roberts, J.L., 1995. Electrochemistry for Chemists, 2nd ed. Wiley-Interscience.
- Schaback, R., 1995. Error estimates and condition numbers for radial basis function interpolation. Adv. Comput. Math. 3 (3), 251–264.
- Seybold, C.A., Mersie, W., Huang, J., McNamee, C., 2002. Soil redox, pH, temperature, and water-table patterns of a freshwater tidal wetland. Wetlands 22 (1), 149–158.
- Shoemaker, C., Kroger, R., Reese, B., Pierce, S.C., 2013. Continuous, short-interval redox data loggers: verification and setup considerations. Environ. Sci. Processes Impacts 15, 1685–1691. https://doi.org/10.1039/c3em00036b.
- Smith, K., van Huyssteen, C.W., 2011. The effect of degree and duration of water saturation on selected redox indicators: pe, Fe2+ and Mn2+. S. Afr. J. Plant Soil 28 (2), 119–126. https://doi.org/10.1080/02571862.2011.10640022.
- Snyder, M., Taillefert, M., Ruppel, C., 2004. Redox zonation at the saline-influenced boundaries of a permeable surficial aquifer: effects of physical forcing on the biogeochemical cycling of iron and manganese. J. Hydrol. 296, 164–178. https:// doi.org/10.1016/j.jhydrol.2004.03.019.
- Soltanian, M.R., Ritzi, R.W., 2014. A new method for analysis of variance of the hydraulic and reactive attributes of aquifers as linked to hierarchical and multiscaled sedimentary architecture. Water Resour. Res. 50(12). https://doi.org/10.1002/201 4WR015468
- Spieker, A.M., 1968. Ground-Water Hydrology and Geology of the Lower Great Miami River Valley Ohio. U. S. G. P. Office.
- Stegen, J.C., Goldman, A.E., Blackburn, S.E., Chu, R.K., Danczak, R.E., Garayburu-Caruso, V.A., Graham, E.B., Grieshauber, C., Lin, X., Morad, J.W., Ren, H., Renteria, L., Resch, C.T., Tfaily, M., Tolic, N., Toyoda, J.G., Wells, J.R., Znotinas, K.R., Brooks, S.C., Bouskill, N.J., Newcomer, M., Rowe, A.R., Saify, A., Smith, G., Soltanian, M.R., Trustschel, L.R., Turetcaia, A., 2018. WHONDRS Surface Water Sampling for Metabolite Biogeography. https://doi.org/10.15485/1484811.
- Su, X., Lu, S., Yuan, W., Woo, N.C., Dai, Z., Dong, W., Du, S., Zhang, X., 2018. Redox zonation for different groundwater flow paths during bank filtration: a case study at Liao River, Shenyang, northeastern China. Hydrogeol. J. 26, 1573–1589. https://doi.org/10.1007/s10040-018-1759-5.
- Swerhone, G.D.W., Lawrence, J.R., Richards, J.G., Hendry, M.J., 1999. Construction and testing of a durable platinum wire eh electrode for in situ redox measurements in the subsurface. Groundwater Monit. Remed. 19 (2), 132–136. https://doi.org/10.1111/i.1745-6592.1999.tb00214.x.

- Torrence, C., Webster, P.J., 1999. Interdecadal Changes in the ENSO-Monsoon System.
 J. Clim. 12 (8), 2679–2690. https://doi.org/10.1175/1520-0442(1999)012 2679:
 ICITEM 2.0.CO;2.
- Vorenhout, M., van der Geest, H.G., van Harum, D., Wattel, K., Eijsackers, H.J.P., 2004. Automated and Continuous Redox Potential Measurements in Soil. J. Environ. Qual. 33, 1562–1567.
- Wallace, C.D., Sawyer, A.H., Barnes, R.T., 2018. Spectral analysis of continuous redox data reveals geochemical dynamics near the stream-aquifer interface. Hydrol. Process. 33 (3), 405–413. https://doi.org/10.1002/hyp.13335.
- Wallace, C.D., Sawyer, A.H., Barnes, R.T., Soltanian, M.R., Gabor, R.S., Wilkins, M.J., Moore, M.T., 2020. A model analysis of the tidal engine that drive nitrogen cycling in coastal riparian aquifers. Water Resour. Res. 56 (4) https://doi.org/10.1029/ 2019WR025662.
- Wallace, C.D., Sawyer, A.H., Soltanian, M.R., Barnes, R.T., 2020. Nitrate removal within heterogeneous riparian aquifers under tidal influence. Geophys. Res. Lett. 47 (10) https://doi.org/10.1029/2019GL085699.
- Wallace, C.D., Soltanian, M.R., 2021. Surface water-groundwater exchange dynamics in buried-valley aquifer systems. Hydrol. Processes. https://doi.org/10.1002/hyp .14066.
- Watkins, J.S., Spieker, A.M., 1971. Seismic Refraction Survey of Pleistocene Drainage Channels in the Lower Great Miami River Valley, Ohio (Ground Water in the Lower Great Miami River Valley, Ohio, Issue. U. S. G. P. Office.
- White, T., Brantley, S., Banwart, S., Chorover, J., Dietrich, W., Derry, L., Lohse, K., Anderson, S., Aufdenkampe, A., Bales, R., Kumar, P., Richter, D., McDowell, B., 2015. Chapter 2 - The Role of Critical Zone Observatories in Critical Zone Science. Developments in Earth Syst. Processes, 19, 15-78. https://doi.org/10.1016/B978-0-444-63369-9.00002-1.
- Xu, F., Liu, Y., Zachara, J., Bowden, M., Kennedy, D., Plymale, A.E., Liu, C., 2017. Redox transformation and reductive immobilization of Cr(VI) in the Columbia River hyporheic zone sediments. J. Hydrol. 555, 278–287. https://doi.org/10.1016/j. jhydrol.2017.10.016.
- Yao, G., Bliss, K.M., Crimi, M., Fowler, K.R., Clark-Stone, J., Li, W., Evans, P.J., 2016. Radial basis function simulation of slow-release permanganate for groundwater remediation via oxidation. J. Comput. Appl. Math. 307, 235–247. https://doi.org/ 10.1016/j.cam.2016.02.006.
- Zhang, J., Zhang, X., Niu, J., Hu, B.X., Soltanian, M.R., Qiu, H., Yang, L., 2019. Prediction of groundwater level in seashore reclaimed land using wavelet and artificial neural network-based hybrid model. J. Hydrol. 577 https://doi.org/10.1016/j. ihydrol.2019.123948.